

# JGR Atmospheres

## RESEARCH ARTICLE

10.1029/2023JD039878

### Key Points:

- Dropsondes over the northwest Atlantic are used to determine mixed layer height (MLH) and boundary layer height (PBLH)
- HSRL-2 lidar MLH product compares well with dropsonde-derived MLH but does not correspond to PBLH for decoupled PBL
- The current operational HSRL-2 algorithm is modified to include retrieval of the PBLH for decoupled PBL

### Supporting Information:

Supporting Information may be found in the online version of this article.

### Correspondence to:

Y. Xu,  
[yikexu@arizona.edu](mailto:yikexu@arizona.edu)

















### Citation:

Xu, Y., Mitchell, B., Delgado, R., Ouyed, A., Crosbie, E., Cutler, L., et al. (2024). Boundary layer structures over the northwest Atlantic derived from airborne high spectral resolution lidar and dropsonde measurements during the ACTIVATE campaign. *Journal of Geophysical Research: Atmospheres*, 129, e2023JD039878. <https://doi.org/10.1029/2023JD039878>

Received 26 AUG 2023

Accepted 26 APR 2024

## Boundary Layer Structures Over the Northwest Atlantic Derived From Airborne High Spectral Resolution Lidar and Dropsonde Measurements During the ACTIVATE Campaign

Y. Xu<sup>1</sup> , B. Mitchell<sup>1</sup>, R. Delgado<sup>1</sup>, A. Ouyed<sup>1</sup>, E. Crosbie<sup>2,3</sup> , L. Cutler<sup>1</sup> , M. Fenn<sup>2</sup> , R. Ferrare<sup>2</sup> , J. Hair<sup>2</sup> , C. Hostetler<sup>2</sup> , S. Kirschler<sup>4,5</sup> , M. Kleb<sup>2</sup> , A. Nehrir<sup>2</sup> , D. Painemal<sup>2</sup> , C. E. Robinson<sup>2</sup>, A. J. Scarino<sup>2</sup>, T. Shingler<sup>2</sup>, M. A. Shook<sup>2</sup> , A. Sorooshian<sup>1,6</sup>, K. L. Thornhill<sup>2</sup> , C. Voigt<sup>4,5</sup> , H. Wang<sup>7</sup> , X. Zeng<sup>1</sup>, and P. Zuidema<sup>8</sup> 

<sup>1</sup>Department of Hydrology and Atmospheric Sciences, University of Arizona, Tucson, AZ, USA, <sup>2</sup>NASA Langley Research Center, Hampton, VA, USA, <sup>3</sup>Analytical Mechanics Associates, Inc., Hampton, VA, USA, <sup>4</sup>Institut für Physik der Atmosphäre, Deutsches Zentrum für Luft- und Raumfahrt (DLR), Wessling, Germany, <sup>5</sup>Institut für Physik der Atmosphäre, Johannes Gutenberg-Universität, Mainz, Germany, <sup>6</sup>Department of Chemical and Environmental Engineering, University of Arizona, Tucson, AZ, USA, <sup>7</sup>Atmospheric Sciences and Global Change Division, Pacific Northwest National Laboratory, Richland, WA, USA, <sup>8</sup>Department of Atmospheric Sciences, Rosenstiel School, University of Miami, Miami, FL, USA

**Abstract** The Planetary Boundary Layer height (PBLH) is essential for studying PBL and ocean-atmosphere interactions. Marine PBL is usually defined to include a mixed layer (ML) and a capping inversion layer. The ML height (MLH) estimated from the measurements of aerosol backscatter by a lidar was usually compared with PBLH determined from radiosondes/dropsondes in the past, as the PBLH is usually similar to MLH in nature. However, PBLH can be much greater than MLH for decoupled PBL. Here we evaluate the retrieved MLH from an airborne lidar (HSRL-2) by utilizing 506 co-located dropsondes during the ACTIVATE field campaign over the Northwest Atlantic from 2020 to 2022. First, we define and determine the MLH and PBLH from the temperature and humidity profiles of each dropsonde, and find that the MLH values from HSRL-2 and dropsondes agree well with each other, with a coefficient of determination of 0.66 and median difference of 18 m. In contrast, the HSRL-2 MLH data do not correspond to dropsonde-derived PBLH, with a median difference of  $-47$  m. Therefore, we modify the current operational and automated HSRL-2 wavelet-based algorithm for PBLH retrieval, decreasing the median difference significantly to  $-8$  m. Further data analysis indicates that these conclusions remain the same for cases with higher or lower cloud fractions, and for decoupled PBLs. These results demonstrate the potential of using HSRL-2 aerosol backscatter data to estimate both marine MLH and PBLH and suggest that lidar-derived MLH should be compared with radiosonde/dropsonde-determined MLH (not PBLH) in general.

**Plain Language Summary** The Planetary Boundary Layer Height (PBLH) is essential for studying the lower atmosphere and its interaction with the surface. Usually, it contains a mixed layer (ML) with vertically well-mixed (i.e., nearly constant) specific humidity and potential temperature. Over the ocean, the PBL is usually coupled (vertically well-mixed) and the ML height (MLH) is usually close to PBLH, hence the MLH estimated from the measurements of aerosol backscatter by a lidar is traditionally compared with PBLH determined from radiosondes/dropsondes. However, when the PBL is decoupled (not vertically well mixed), the MLH differs from the PBLH. Here we used dropsondes' thermodynamic profile to evaluate the airborne High-Spectral-Resolution Lidar—Generation 2 (HSRL-2) estimation of MLH and PBLH in airborne field campaign over the northwestern Atlantic (ACTIVATE) from 2020 to 2022. We show that the HSRL-2 has excellent MLH estimation compared to the dropsondes. We also improved the HSRL-2 estimation of PBLH. Further data analysis indicates that these conclusions remain the same for cases with different cloud fractions, and for decoupled PBLs. These results demonstrate the potential of using HSRL-2 aerosol backscatter data to estimate both marine MLH and PBLH and suggest that lidar-derived MLH should be compared with radiosonde/dropsonde-determined MLH (not PBLH) in general.

## 1. Introduction

The planetary boundary layer (PBL) is the lowest layer of the atmosphere and it has direct effects on global weather and climate as it interacts with the planet's surface and is also the layer of the atmosphere where humans reside (Teixeira et al., 2020). The height of PBL (PBLH) varies depending on the seasonal cycle, diurnal solar heating, and low-level cloud-top cooling, and the estimation of PBLH has received much attention in recent years (Palm et al., 2021; Teixeira et al., 2020).

Over the ocean, the marine PBL is usually statically unstable (with near-surface virtual potential temperature decreasing with height), consisting of a well-mixed layer and a capping inversion, with the PBLH usually greater than (or close to) the mixed layer (ML) height (MLH). When low-level clouds exist, the MLH is usually defined as the cloud base, while the cloud top is defined as the PBLH, suggesting that PBLH can be much greater than MLH (Zeng et al., 2004). PBLH can also be greater than MLH for a decoupled PBL in which a shallow ML is decoupled from the upper part of PBL (Jones et al., 2011). For instance, the decoupled PBL is often found downwind of subtropical stratocumulus clouds when turbulence is insufficient to maintain a well-mixed PBL, particularly when the PBLH is over 1 km (Bretherton & Wyant, 1997; Jones et al., 2011; Luo et al., 2016; Wood & Bretherton, 2004; Zuidema et al., 2009).

A challenge to understand marine PBL structure and its associated processes is the scarcity of observational data (Teixeira et al., 2020). One well-known method to estimate PBLH variability over ocean is through the use of spaceborne lidar. For example, CALIPSO (Cloud-Aerosol Lidar and Infrared Pathfinder Satellite Observation) is the first spaceborne polarized lidar for aerosol and cloud measurement, from which the aerosol distributions can be used to estimate MLH (Hunt et al., 2009; Luo et al., 2016). The ICESat-2 (Ice, Cloud, and land Elevation Satellite) lidar (Neumann et al., 2019) does not provide a PBLH product but there have been multiple proposed MLH retrievals using ICESat-2 aerosol backscattering (Palm et al., 2021). Because MLH and PBLH can sometimes coincide, MLH (e.g., from lidar measurements) has also been used to represent PBLH (e.g., in model evaluations) (Brunke et al., 2022; Caicedo et al., 2019; Hegarty et al., 2018; Liu et al., 2023; Scarino et al., 2014; Teixeira et al., 2020). More advanced lidars are widely used in airborne field campaigns, including their use for estimating MLH. For instance, the NASA Langley Research Center (LaRC) airborne High Spectral Resolution Lidar-Generation 2 (HSRL-2) has been used in various field campaigns to retrieve the vertical distribution of aerosol properties and estimate MLH in cloud free conditions over land (Liu et al., 2023; Scarino et al., 2014). Although the laser beam cannot penetrate thick clouds, there are usually holes between clouds where MLH can still be retrieved.

Radiosondes are commonly used to derive PBLH (Teixeira et al., 2020). For instance, Scarino et al. (2014) used ceilometers and radiosondes to evaluate the HSRL's estimate of MLH. These comparisons of lidar-estimated MLH and radiosonde/dropsonde-derived PBLH are appropriate most of the time, as the PBLH is usually similar to MLH in nature. However, PBLH can be much greater than MLH for decoupled PBLs, and such comparisons would lead to larger differences. In this study, we will quantitatively address this issue using dropsonde data from research flights between 2020 and 2022 over the Northwest Atlantic. First, we will use the dropsonde data to estimate both MLH and PBLH and quantify their differences. Then we will assess the relationship between HSRL-2's MLH product and dropsonde MLH and PBLH and quantify the differences if the HSRL-2's MLH is used to represent marine PBLH. With insights gained from these data analyses, we present a slightly revised HSRL-2 MLH retrieval for an automatic PBLH retrieval, demonstrating the potential of using HSRL-2 aerosol backscatter data to estimate both marine MLH and PBLH.

## 2. Data and Methods

### 2.1. Dropsonde and HSRL-2 Data

The dropsonde and HSRL-2 data were collected during the Aerosol Cloud meteorology Interactions over the western Atlantic Experiment (ACTIVATE) field campaigns (Sorooshian et al., 2019, 2023). ACTIVATE flights were executed mostly in winter and summer for a more extensive coverage of the dynamic range of aerosols and meteorological conditions, as well as different cloud types. ACTIVATE featured joint flights whereby the high-flying NASA LaRC King Air (at an altitude of ~9 km) was spatially coordinated with the low-flying NASA LaRC HU-25 Falcon (at an altitude <3 km), as outlined in Sorooshian et al. (2023). This research exclusively utilized the data collected by the HSRL-2 (Hair et al., 2008) and the National Center for Atmospheric Research (NCAR)

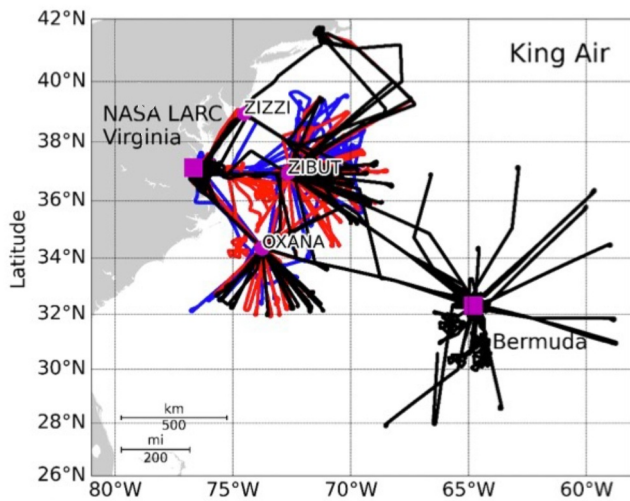


**Figure 1.** The King Air flight routes from 2020 to 2022 (blue = 2020, red = 2021, black = 2022). All flights took place during the day (adopted from Sorooshian et al. (2023)).

nRD41 mini-sondes (dropsondes) (Vömel et al., 2023) through the Airborne Vertical Atmospheric Profiling System (AVAPS) by the King Air aircraft. The multi-wavelength airborne HSRL-2 provides vertically resolved aerosol properties. All flights were during day time. There are three different flight paths used to release the dropsondes: (a) a circle and spoke patterns of sondes launched around a point, (b) flights under a satellite overpass, and (c) flights out to a point and return (Sorooshian et al., 2023). Figure 1 shows all of the King Air flight tracks in the region covered by the ACTIVATE flights.

The HSRL-2's MLH is retrieved using a wavelet-based algorithm applied to the 532 nm aerosol backscatter product for all 3 years of ACTIVATE (2020–2022) using a fixed set of retrieval parameters (see Section 2.3). Scarino et al. (2014) used ceilometers and radiosondes to evaluate the HSRL's MLH and showed good agreement of MLH with a bias lower than 50 m and a correlation coefficient greater than 0.9 over land in the Central Valley and over the foothills of the Sierra Nevada, California.

Furthermore, we will use an additional product (MLH-LaRC) (for the year 2020 only) that was produced by combining the above automatic algorithm with manual inspection (Scarino et al., 2014). Specifically, every curtain of backscatter profiles in 2020 was visually inspected first. If the automated

algorithm chooses an edge gradient that does not appear to be associated with the MLH, the threshold retrieval parameter is adjusted to match the visual inspection (Scarino et al., 2014). The MLH values determined from the automated algorithm and from the manual inspection are combined to produce a set of “best estimate” MLH, equal to the automated estimate where they agree within 300 m, and equals to the manual otherwise (Scarino et al., 2014). While this adjustment process is subjective, the evaluation of this experimental product may provide some insights for the further improvement of the automatic algorithm.

It takes ~10 min for a dropsonde to reach the surface from the aircraft altitude (~9 km). To collocate the HSRL-2 and dropsondes, we choose the MLH with the closest distance to the dropsonde. In this way, we are able to use 506 dropsondes (out of 785 dropsondes) with collocated HSRL-2 MLH data within about 20 km in the horizontal distance in this study. Conclusions remain the same if a 10, 30, or 40 km horizontal distance is used (results not shown).

In the discussion of the comparison results, we also use HSRL-2 low cloud fraction (CF) determined at the 506 collocated datapoints: For our focus on low clouds, we use the average CF in the lowest 3 km above the surface that fell within the 10-min interval. Specifically, CF for each dropsonde is calculated using the HSRL-2 cloud\_top\_height variable and the dropsonde data. First, the dropsonde launch time is matched to the corresponding time in the HSRL-2 data. Then, plus or minus 5 min from the dropsonde launch time are identified to create a 10-min interval. Within the 10-min interval, every measurement with a cloud top height of less than 3 km is counted, divided by the total number of measurements within the 10-min interval to calculate the CF.

## 2.2. MLH and PBLH Derivations From Dropsonde Thermodynamic Profiles

First, it is important to identify the difference between ML and PBL. The ML represents the layer with vertically well-mixed (i.e., nearly constant) virtual potential temperature and specific humidity. For coupled (i.e., well mixed) PBLs (Figures 2a and 2b), the PBL includes the ML and the thin capping inversion, and hence MLH is close to PBLH. For decoupled PBLs (Figures 2a and 2c), MLH is the cloud base, while PBLH is the cloud top, leading to a much greater PBLH than MLH.

Motivated by the above schematic features of coupled versus decoupled PBLs and the thermodynamic profiles from the dropsondes in Figure 2, we have developed an algorithm to estimate the PBLH and MLH from dropsonde profiles. Figure 3 shows the steps to determine PBLH and MLH from the dropsonde thermodynamic profiles with a vertical interval of around 7 m. As the marine PBL is usually statically unstable (with a well-defined mixed layer), we focus on unstable PBL cases using the algorithm in Figure 3. The PBL is defined as stable if the maximum virtual potential temperature ( $\theta_v$ ) from the lowest ~70 m above the ocean is less than the minimum  $\theta_v$  from the bottom 10th to 20th points (lowest ~70–~140 m). The stable PBLs represent only 14% of

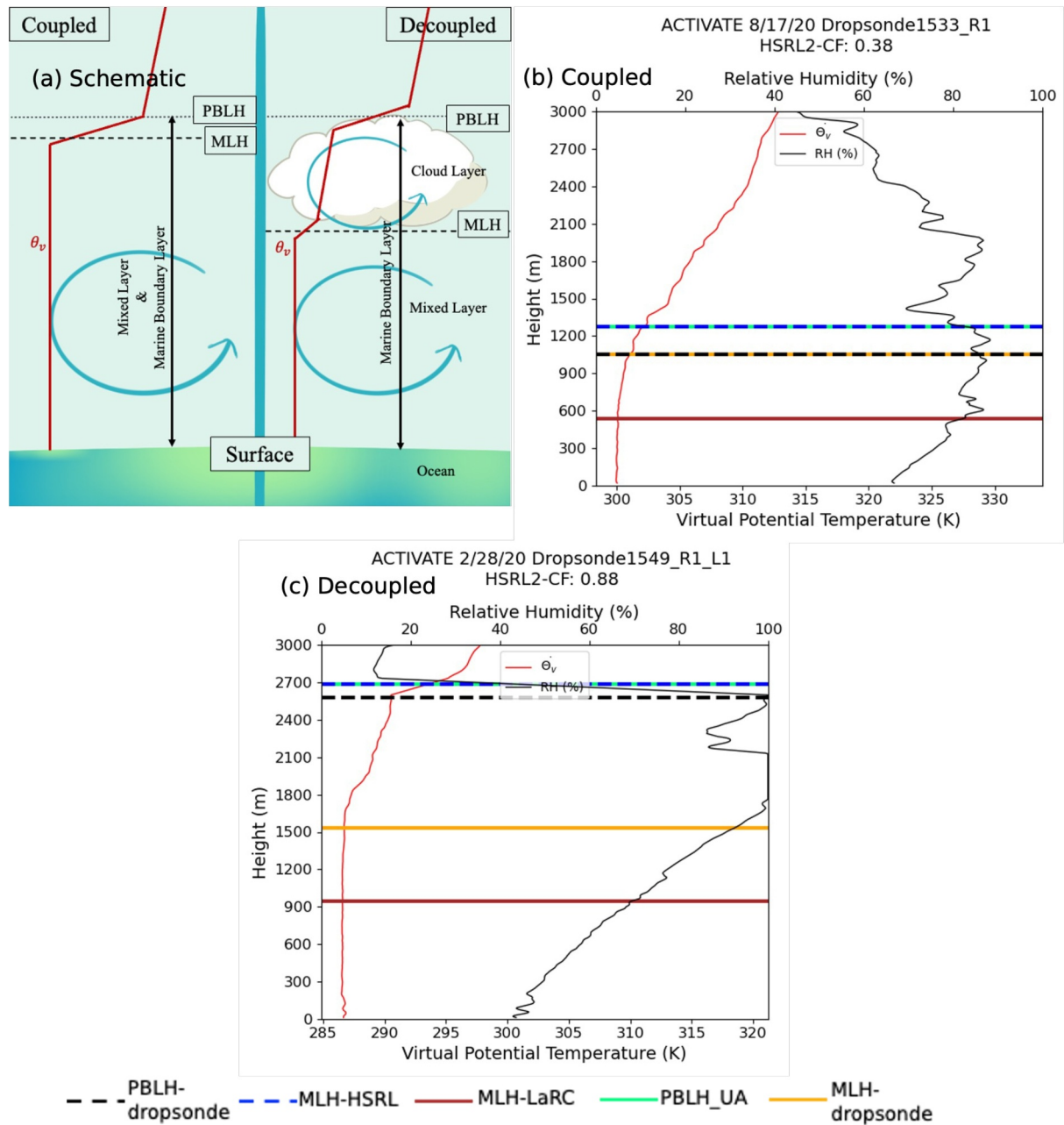


**Figure 2.** (a) The schematic of coupled (i.e., well mixed) versus decoupled PBLs over the ocean, where the PBLH and MLH are close to each other for coupled PBLs, and far away from each other for decoupled PBLs. The red lines show the typical  $\theta_v$  profile. (b) Example of a coupled PBL. (c) Example of a decouple PBL.

the dropsondes (see Section 3.1) and are shallow (see Figure S1b in Supporting Information S1). Additional efforts are needed to develop an algorithm (different from that in Figure 3) to reliably compute PBLH from dropsonde data for stable PBLs. Furthermore, the aerosol gradient may be small or non-existent at PBLH for stable PBLs because aerosols may be confined to the bottom of stable PBLs, making the lidar estimation less reliable as a proxy of the PBLH. For these reasons, we leave stable PBLs as a future task.

For our algorithm in Figure 3, we first eliminate cases that do not reach a minimum altitude of 40 m (step 1, Figure S1a in Supporting Information S1) and cases that are stable (step 1, Figure S1b in Supporting Information S1)—output as no data (Nan). Second, we estimate if a boundary layer cloud is present (Step 3) by having relative humidity (RH) exceeding 95% above the lifting condensation level (LCL, determined from temperature and dewpoint from 100 m above the surface) within 3,000 m above the surface (Zeng et al., 2004). If there is a cloud

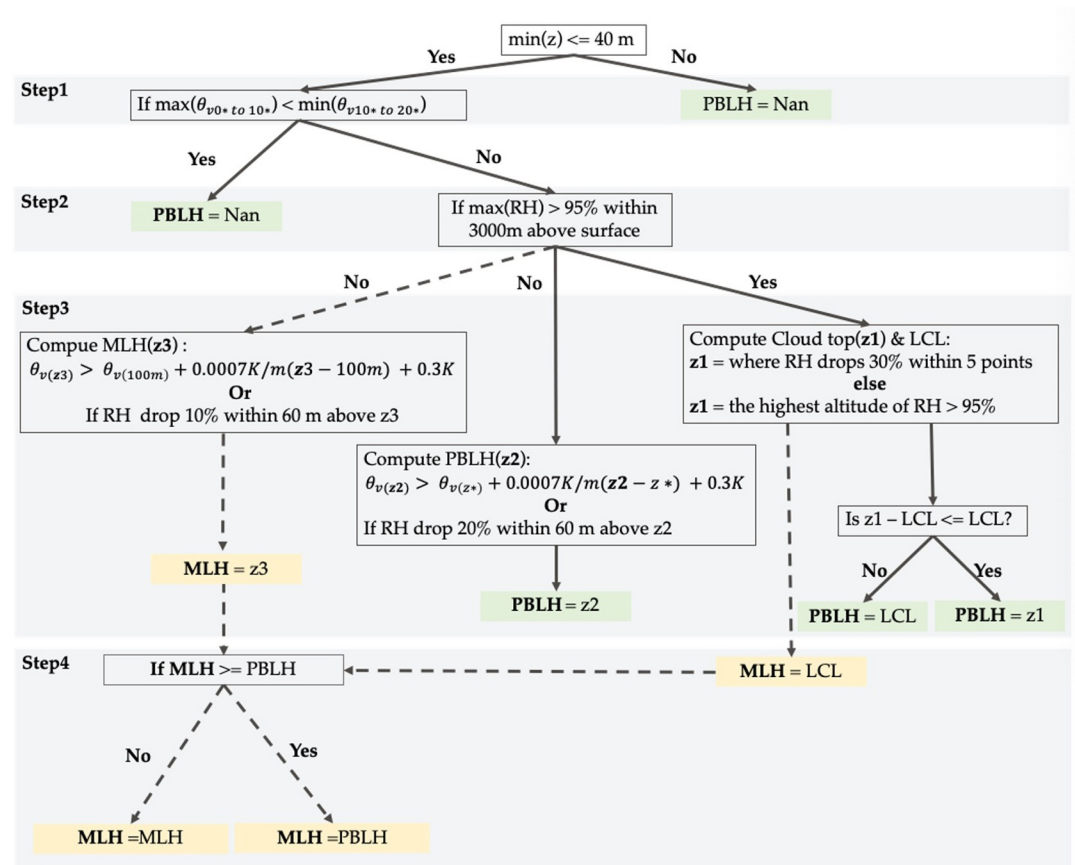


**Figure 3.** The steps to determine PBLH from the dropsonde thermodynamic profiles. The steps are the same for determining MLH by taking  $z_0 = 100$  m (dashed lines). LCL refers to lifting condensation level.  $\theta_v$  refers to the virtual potential temperature. RH refers to relative humidity.  $\theta_{v0^*}$  refers to the bottom point in the  $\theta_v$  profile, and  $\theta_{v10^*}$  refers to the 10th point ( $\sim 100$  m) from bottom up.  $z^*$  refers to the altitude where  $\theta_v$  is the greatest value among the bottom six points in the profile, starting from the surface up.

(step 3 (right)), the altitude ( $z_1$ ) is set to cloud top or the point where there is a sudden drop in RH, and the results are not sensitive to the exact constant values (e.g.,  $>30\%$  RH drop within 5 points) used (Figure S2 in Supporting Information S1). We then add a constraint (Zeng et al., 2004) that if the PBL is within a thick cloud ( $z_1 - LCL > LCL$ ), we use the cloud base as the PBLH (Figure S2a in Supporting Information S1); if within a thin cloud ( $z_1 - LCL < LCL$ ), we use the cloud top as the PBLH (Figure S2b in Supporting Information S1). If there is no cloud (step 3 (middle)), the altitude ( $z_2$ ) is determined when we consider the slight increase of  $\theta_v$  with height at a rate of 0.7 K/km due to large eddies (Garratt, 1992) in the unstable marine PBL (Figure S3a in Supporting Information S1), or the RH drop by 20% (Figure S3b in Supporting Information S1). The constant (0.3 K) ensures that the PBL top inversion is reached. To determine the constant (0.3 K), we first manually/visually inspected the 506 dropsonde profiles and generated approximated PBLH values. The constant is determined by looping through values within a reasonable range (0.3–1 K) and obtaining the constant (0.3 K) with the least difference when comparing with the manually determined PBLHs.

The MLH is determined similarly (step 3 (left)), except using starting altitude = 100 m. This is due to the assumption that, for an unstable PBL, the 100 m height is within or near the ML, leading to the base of the inversion layer, while  $\theta_v$  at  $z_0$  is greater than that at 100 m (for an unstable PBL), leading to a PBLH in the inversion layer, which also ensures that  $MLH \leq PBLH$ . An additional step is added to ensure  $MLH \leq PBLH$  (step 4). Physically, our parcel method determines PBLH or MLH as the height at which a near-surface air parcel (for PBLH) or an air parcel in the lower part of the ML moves upward adiabatically to reach the inversion. In this process, the slight increase of  $\theta_v$  with height at a rate of 0.7 K/km due to large eddies (Garratt, 1992) and thick versus thin clouds are also considered.

### 2.3. MLH and PBLH Derivations From HSRL-2

HSRL-2 estimates MLH (denoted as MLH-HSRL) using an automated technique that utilizes a Haar wavelet transform with a dilation value of  $a = 360$  m in Equation 1 below, to identify the sharp gradients in aerosol backscatter profiles, usually located at the top of the ML (the lowest maxima) (Brooks, 2003; Davis et al., 2000; Scarino et al., 2014). The Haar wavelet transform is able to detect the step changes in a lidar signal, whereas the Haar function  $h$  is defined as (Brooks, 2003):

$$h\left(\frac{z-b}{a}\right) = \begin{cases} +1 & : b - \frac{a}{2} \leq z \leq b \\ -1 & : b \leq z \leq b + \frac{a}{2} \\ 0 & : \text{elsewhere} \end{cases} \quad (1)$$

where  $z$  is altitude,  $b$  is the center of the Haar function, and  $a$  is the dilation value (Brooks, 2003). From the Haar function, the covariance transform of the Haar function ( $W_f$ ) between the lower and upper limits of the profile ( $z_b$  and  $z_t$ ) can be calculated from

$$W_f(a, b) = \frac{1}{a} \int_{z_b}^{z_t} f(z) h\left(\frac{z-b}{a}\right) dz \quad (2)$$

A local maximum in  $W_f(a, b)$  identifies the step change in the aerosol backscatter profile  $f(z)$  with a coherent scale of  $a$ , located at  $z = b$ . The key to identifying features of interest is the selection of an appropriate dilation under less ideal conditions (Brooks, 2003). In general,  $W_f(a, b)$  contains more than one local maxima with different magnitudes, and the HSRL algorithm only considers local maxima greater than an empirically determined threshold value. Specifically, MLH is taken as the lowest altitude with the local maximum rather than the altitude with the overall maximum of  $W_f(a, b)$  (Scarino et al., 2014).

It needs to be emphasized that, as widely recognized, the MLH derived from aerosol backscatter profiles is often a good proxy of, but could differ from, the MLH derived from thermodynamic profiles for unstable PBLs. Partly for this reason, as an experimental product, in 2020, the MLH-HSRL was further manually adjusted by tuning the threshold and dilation values in each flight based on visual inspection and MLH climatology (Scarino et al., 2014) in order to retrieve the MLH more accurately. This product is called MLH-LaRC. While the approach is subjective, we take this as an opportunity to evaluate this experimental product in this study, as it may provide some insights for the further improvement of the automatic algorithm.

As mentioned in Section 1, MLH (e.g., from lidar measurements) has also been used to represent PBLH in prior studies, but we find that the MLH-HSRL can differ significantly from PBLH-dropsonde for some cases (see Section 3). Using the insights from these intercomparisons, we revise the MLH-HSRL (automated) algorithm to better retrieve PBLH. The final product is denoted as PBLH-UA. As mentioned above, we make two revisions to the above MLH-HSRL algorithm, as illustrated in Figure 4: (a) decreasing the default dilation value (i.e.,  $a$  in the above two equations) from 360 to 280 m (Figure 4a) through a systematic process of trial and refinement to resolve more peaks; and, more importantly, (b) utilizing both the lowest altitude with the local maximum ( $z_1$ ;  $\sim 700$  m in Figure 4a) and the altitude with the overall maximum ( $z_2$ ;  $\sim 1,200$  m in Figure 4a). When the difference ( $z_2 - z_1$ ) is less than  $z_1$ , we use  $z_2$  for PBLH-UA, which is greater than MLH-HSRL. For other cases, we use  $z_1$  for PBLH-UA, which is similar to MLH-HSRL. When compared with the nearest dropsonde (Figure 4b, with a distance of 16 km), the PBLH-UA picked up the PBLH at  $z_2 = \sim 1,200$  m (instead of the  $z_1 = \sim 700$  m), which is very close to the PBLH-dropsonde. Physically, the vertical profile of the backscatter coefficient (i.e., the right profile in Figure 4a) represents the HSRL2's measurements averaged over a period of 10 s, including both cloudy conditions (where the strongest backscatter is from cloud top) and clear-sky conditions (where the strongest backscatter is from the ML top). Therefore, the profile exhibits two maxima at  $z_2 = \sim 1,200$  m and  $z_1 = \sim 700$  m, consistent with the cloud top and cloud base (as represented by the LCL) from the nearest dropsonde (Figure 4b). As ( $z_2 - z_1$ , representing the cloud thickness) is greater than  $z_1$  (cloud base height), the cloud layer is thin, and  $z_2$  is taken as the PBLH-UA.

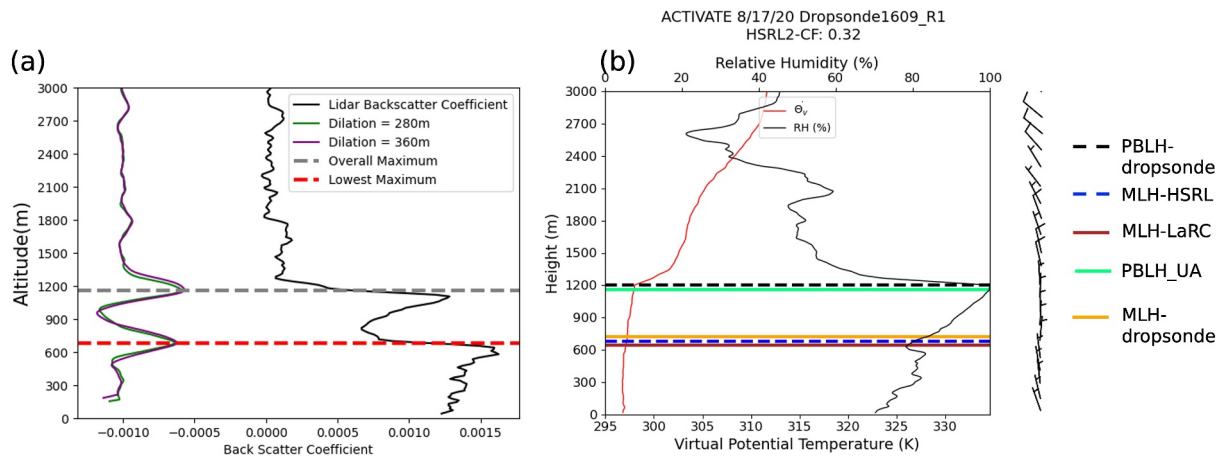


**Figure 4.** The different dilation values used in (a) PBLH-UA (dilation = 280 m) and MLH-HSRL (dilation = 360 m). The line on the right is the particulate backscatter coefficient, and the two overlapped lines on the left are the signal after wavelet transform and shifted 10-3 to the left side of the x-axis. The local maximum of the backscatter coefficient at the lowest altitude and the overall maximum of the backscatter coefficient are also shown. (b) The comparison with the nearest dropsonde's thermodynamic profile. PBLH-UA picks up the overall maximum at 1,200 m, which is in agreement with the dropsonde.

For the evaluations of these three products, we use three statistical metrics: the coefficient of determination ( $R^2$ ), the median, and the interquartile range (IQR, i.e., the difference between 75th and 25th percentiles of differences). In general, the median and IQR values are more robust statistical metrics (against outliers) than mean differences, root mean square differences, and mean absolute differences.

### 3. Results

#### 3.1. Marine Daytime MLH and PBLH From Drospondes

First, we use the dropsonde data to compare marine daytime MLH and PBLH. Usually, they are close to each other (e.g., Figure 2; Figure S2a in Supporting Information S1). Sometimes, MLH is considerably lower than PBLH (Figure 2; Figure S2b in Supporting Information S1). Furthermore, PBLH and MLH are affected by weather patterns, and different seasons are associated with different weather patterns (Tornow et al., 2023). Therefore, Figure 5 shows the seasonal cycle of PBLH and MLH from dropsonde data. PBLH and MLH are higher in the winter months (January, February, and March) than in other months (Figure 5a), because the PBL is more statically unstable in winter. The PBLH and MLH differences are also greater in winter than in other months (Figure 5a). One reason is the greater cloud fractions in winter (Figure 5b). With a deeper PBL in winter, these clouds would also be thicker. As MLH and PBLH are close to the cloud base and top, respectively, their differences are also greater in winter.

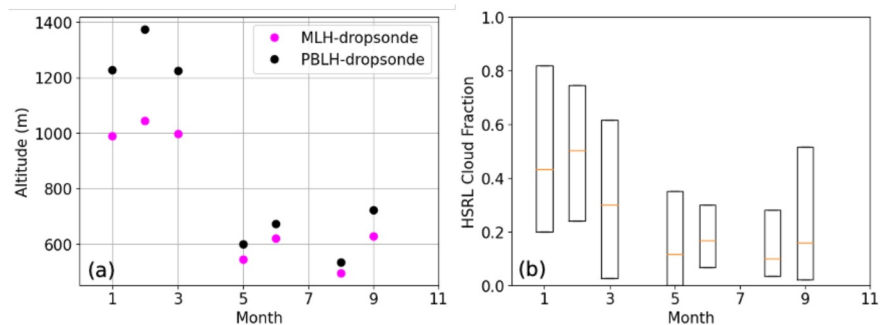


**Figure 5.** (a) The monthly median value (m) of PBLH and MLH from dropsondes in 2020–2022; and (b) the monthly 25th, 50th (median), and 75th of HSRL-2 cloud fraction. April, November, and December are dropped due to small number of cases (<15). The number of dropsondes in each month: January (41), February (46), March (111), April (2), May (64), June (142), July (0), August (37), September (46), November (3), December (14).

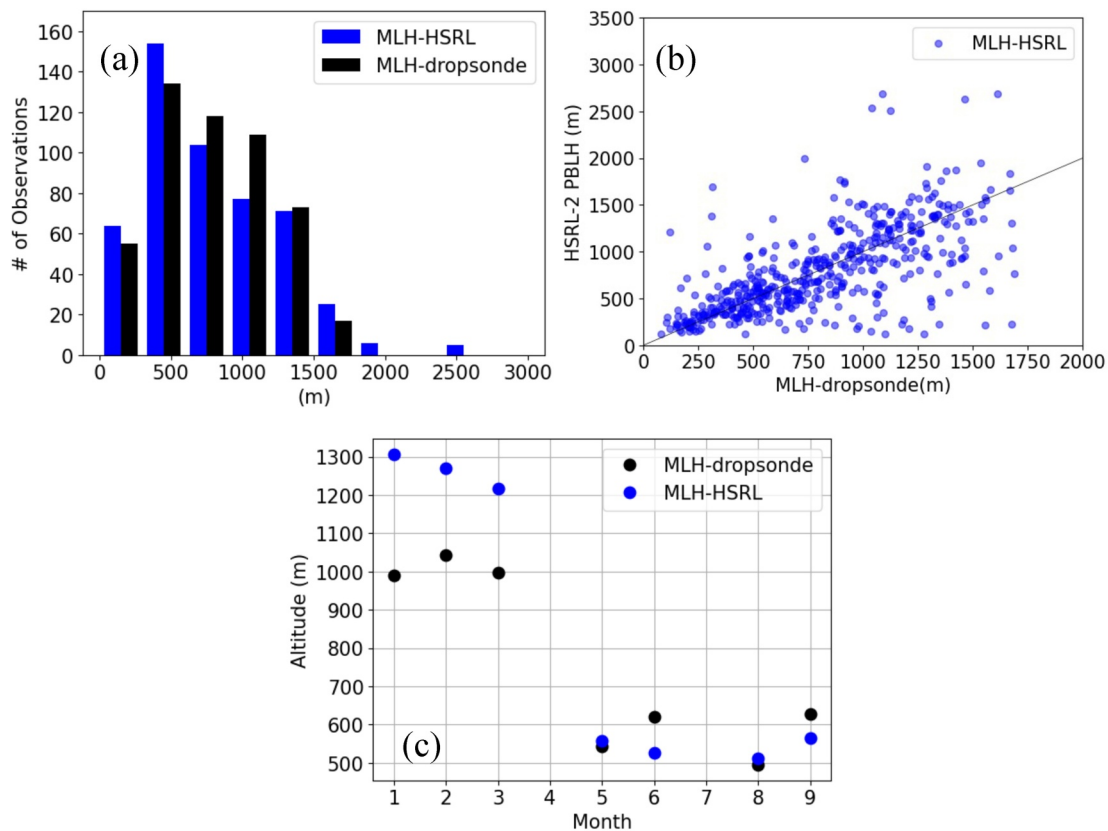


**Figure 6.** (a) The distribution of MLH-HSRL versus MLH-dropsonde using all data from 2020 to 2022. Data are binned every 300 m from 0 to 3,000 m. (b) Scatterplot of lidar-estimated MLH versus MLH-dropsondes. The black line is the 1:1 line. (c) Monthly medians. April, November, and December results are not shown in panel (c) as there are less than 15 dropsondes collocated with HSRL-2 MLH data.

To evaluate the HSRL-retrieved MLH and PBLH using the co-located dropsonde data, we use the HSRL data within a radius of 20 km around a dropsonde. With this co-location criterion, there are 610 dropsondes out of a total of 785 dropsondes launched from 2020 to 2022. Further, 104 dropsondes are excluded from the analysis, including 87 stable cases and 17 cases in which the lowest altitude of the dropsonde was above 40 m, resulting in 506 dropsondes used in the analysis below.

### 3.2. Relationship of HSRL-2 MLH With Dropsonde MLH and PBLH

MLH-HSRL is the product based on an automated retrieval algorithm (Section 2.3). Figure 6 demonstrates that MLH-HSRL agrees well with MLH-dropsonde in terms of the distributions in altitude bins, variation from month to month, and even spread around the 1-1 line. Figure 6c shows that MLH-HSRL has larger differences from MLH-dropsonde in winter months than in other months. The monthly difference between MLH-HSRL versus MLH-dropsonde could be due to the clouds at the top of the ML or complicated aerosol structures within and/or above the ML (Scarino et al., 2014). For the whole period, Table 1 shows that MLH-HSRL has an  $R^2$  of 0.44 with MLH-dropsonde, and median and IQR of differences of 18 and 286 m, respectively.

Because MLH-dropsonde sometimes differs from PBLH-dropsonde (see Section 3.1) and MLH-HSRL was used to represent PBLH in prior studies over land (e.g., Caicedo et al., 2019; Hegarty et al., 2018; Liu et al., 2023; Scarino et al., 2014), it is useful to also compare MLH-HSRL against PBLH-dropsonde. For most months, MLH-HSRL is less than PBLH-dropsonde (Figure 7c), with a median difference of  $-47$  m (Table 1), which is larger in magnitude than compared with MLH-dropsonde ( $-8$  m, Table 1). Motivated by the larger differences (between MLH-HSRL and PBLH-dropsonde) and considering the need to use an automated algorithm for future satellite missions in global applications, we conducted sensitivity tests using the MLH-HSRL algorithm and developed the automated PBLH-UA algorithm by revising the MLH-HSRL algorithm (see Section 2.3). PBLH-UA agrees better with PBLH-dropsonde than MLH-HSRL in terms of most of the altitude bins (Figure 7a), scatter plots



**Table 1**  
*Statistical Metrics When Comparing MLH-HSRL Against Dropsonde-Derived MLH and PBLH in 2020–2022*

	$R^2$	Median difference (m) with dropsondes	IQR difference (m) with dropsondes
2020–2022 MLH			
MLH-HSRL	0.44	18	286
PBLH-UA	0.45	53	295
2020–2022 PBLH			
MLH-HSRL	0.42	−47	296
PBLH-UA	0.48	−8	242

(Figure 7b), and winter months (Figure 7c). Accordingly, Table 1 shows that PBLH-UA shows a higher correlation and much better median difference (−8 m vs. −47 m) and IQR (242 vs. 296 m).

#### 4. Discussion

As shown in Section 3.1, PBLH-dropsonde and MLH-dropsonde differ sometimes. Due to the importance of PBLH and MLH relation with cloud fraction (CF) for the understanding of cloud processes, it is interesting to consider how their differences vary with cloud fraction which is related to different weather patterns. Figure 8 shows that both PBLH and MLH increase with greater low cloud fractions, with an  $R^2$  value that is statistically significant ( $p$ -value < 0.01). The PBLH has a greater slope (black line) when compared with that of MLH (pink line), with a higher  $R^2$  value (0.31 vs. 0.20).

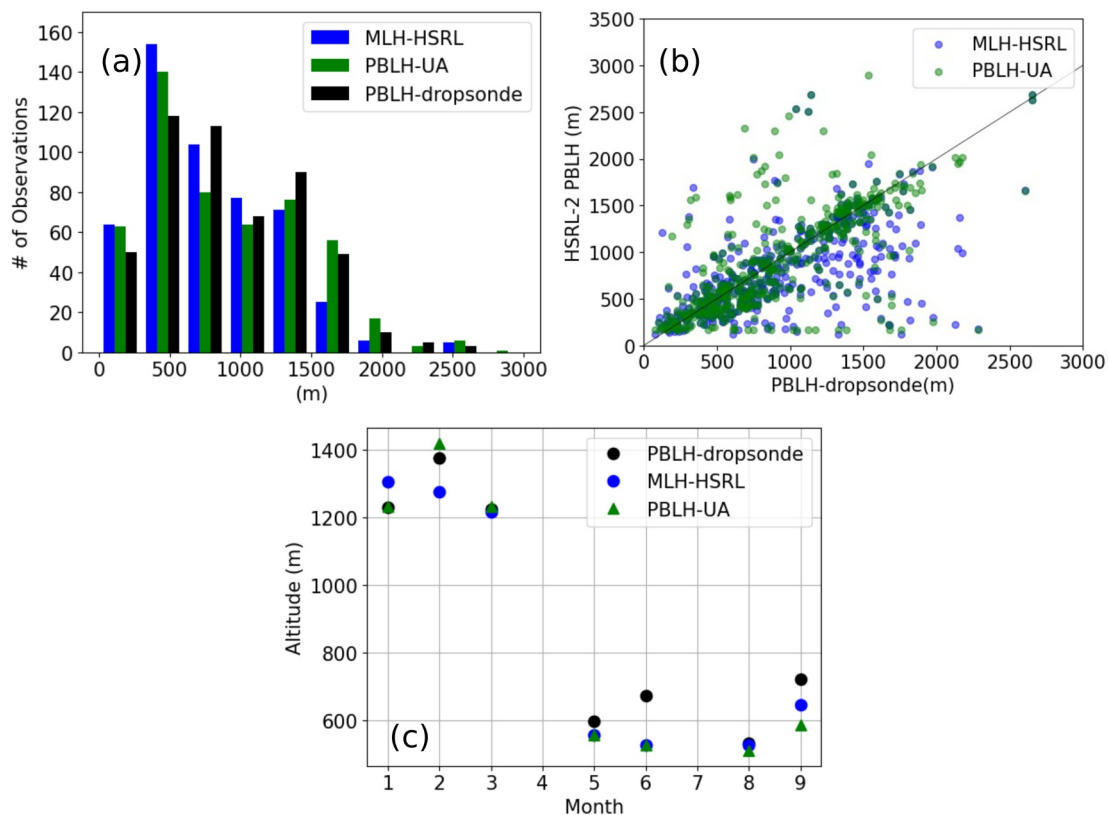


**Figure 7.** (a) The distribution of MLH-HSRL, PBLH-UA, and PBLH-dropsonde. Data are binned every 300 m from 0 to 3,000 m. (b) Scatter of lidar-estimated PBLH versus PBLH-dropsondes. The black line is the 1:1 line. (c) Monthly medians. April, November, and December results are not shown in panel (c) as there are less than 15 dropsondes collocated with HSRL-2 MLH data.

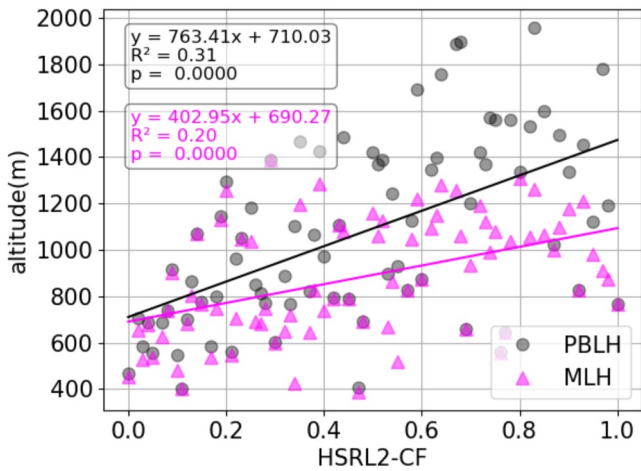


**Figure 8.** The medians of PBLH-dropsonde (black) and MLH-dropsonde (pink) at each HSRL-2-CF value versus HSRL-2 low cloud fractions. The HSRL-2-CF values are initially rounded to the closest 0.01. Subsequently, the medians of the PBLH-dropsonde and MLH-dropsonde in each 0.01 CF bin are calculated and graphed on a scatterplot.

As the median cloud fraction is 0.22 using all dropsondes, we have also computed the statistics for  $CF \leq 0.22$  and  $CF > 0.22$  separately. When CF is less than or equal to 0.22 the PBLH-dropsonde median value (659 m) does not differ much from MLH-dropsonde (624 m), with a difference of 34 m. Compared with PBLH-dropsonde, PBLH-UA has better performance than MLH-HSRL, with a lower median difference ( $-2$  m vs.  $-24$  m) in magnitude. When CF is greater than 0.22, the median value for PBLH-dropsonde (1,169 m) is greater than MLH-dropsonde (950 m), and this difference (218 m) is much greater than that (34 m) for  $CF \leq 0.22$ . Overall, it is evident that an increase in low cloud fraction leads to a wider separation between the PBLH-dropsonde and MLH-dropsonde. Compared with PBLH-dropsonde, PBLH-UA outperforms MLH-HSRL, with a lower median difference ( $-14$  m vs.  $-74$  m) in magnitude.

Besides cloud fraction, another interesting question is how our results will change for decoupled PBLs (e.g., Jones et al., 2011) that have larger PBLH and MLH differences (than well-mixed PBLs). Following the definition of decoupled PBL based on aircraft measurements from Jones et al. (2011), we use a similar criterion for dropsonde data for our sensitivity test. Specifically, if the mean specific humidity difference between the bottom 25% and top 25% of PBL is less than 0.5 g/kg and the mean virtual potential temperature difference between the top 25% and bottom 25% of PBL is less than 0.5 K, the PBL is defined to be well mixed; otherwise, the PBL is defined to be decoupled. Furthermore, we only consider cases with  $PBLH > 400$  m so that there is enough data in the top and bottom 25% of PBL.

Overall, a total of 141 dropsondes out of 506 dropsondes ( $\sim 28\%$ ) have decoupled boundary layers (Figure 9). Figure 9a shows that June has the most decoupled cases (53) than other months because June has the highest number of dropsondes (142, see Figure 5). The decoupled PBLs occurred in 7 months, with greater differences between PBLH-dropsonde and MLH-dropsonde in winter (January, February, and March) than in other months, consistent with the results using all dropsonde data (Figure 5a). For instance, the median differences are 465 m in January and 201 m in August in Figure 9b, and they are larger than those using all data for those months (239 and 39 m in Figure 5a, respectively). This is due to thicker clouds with more synoptic events (cold fronts) and storms in winter over the Atlantic region (Kirschler et al., 2023).

For the decoupled PBL cases, we have also repeated the evaluations in Section 3, and the results are summarized in Table 2. Compared with PBLH-dropsonde, PBLH-UA performs better than MLH-HSRL based on the three metrics, also consistent with the results using all dropsonde data in Table 1. When compared to those using all observations, both PBLH-UA and MLH-HSRL tend to have larger differences from PBLH-dropsonde for decoupled PBLs. For instance, compared with PBLH-dropsonde, MLH-HSRL has a higher median difference

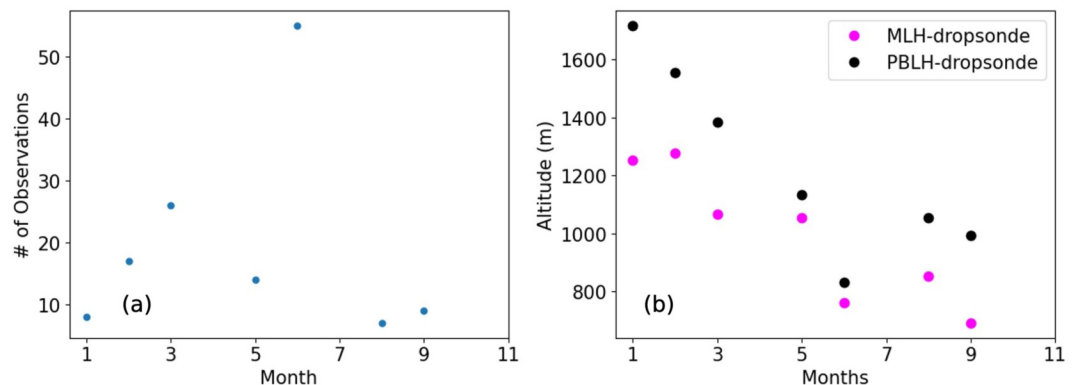


**Figure 9.** (a) The number of monthly cases of decoupled PBLs in 2020–2022, and (b) the corresponding monthly median PBLH and MLH of dropsondes.

**Table 2**  
*Statistical Metrics When Comparing MLH-HSRL and PBLH-UA Against MLH and PBLH of Dropsondes With Decoupled PBLs*

	$R^2$	Median difference (m) with dropsondes	IQR difference (m) with dropsondes
2020–2022 MLH of days with decoupled PBLs			
MLH-HSRL	0.32	−164	388
PBLH-UA	0.3	−75	539
2020–2022 PBLH of days with decoupled PBLs			
MLH-HSRL	0.33	−312	459
PBLH-UA	0.44	−193	315

(−297 m) in magnitude for decoupled PBLs than for all cases (−51 m); PBLH-UA has a higher median difference (−197 m) in magnitude for decoupled PBLs than for all cases (−8 m).

As the median HSRL2-CF is 0.22 for decoupled PBLs, we have also computed the statistics for  $CF \leq 0.22$  and  $CF > 0.22$  separately. When  $CF \leq 0.22$ , the PBLH-dropsonde (932 m) is greater than MLH-dropsonde (874 m). Compared with PBLH-dropsonde, PBLH-UA has a lower median difference (−75 m) in magnitude than MLH-HSRL (−164 m). When CF is greater than 0.22, the PBLH-dropsonde (1,532 m) and MLH-dropsonde (1,011 m) have a much larger difference (521 m). Compared with PBLH-dropsonde, the median difference (−193 m) from PBLH-UA is less than that (−312 m) from MLH-HSRL in magnitude.

Finally, as mentioned in Section 2, both MLH-HSRL (from an automated algorithm) and MLH-LaRC (based on MLH-HSRL and manual correction) data are available for 2020. Here, we also take this opportunity to evaluate the impact of manual correction on the MLH retrieval performance. Compared with MLH-dropsonde, MLH-LaRC outperforms MLH-HSRL with a higher  $R^2$  (0.64 vs. 0.42), lower median difference (27 vs. 40 m), and comparable IQR (249 vs. 256 m) due to manual revision. Compared with PBLH-dropsonde, MLH-LaRC has the highest  $R^2$  (0.58) among the three products (i.e., MLH-LaRC, MLH-HSRL, and PBLH-UA), while PBLH-UA has the lowest median difference (−2 m) in magnitude.

## 5. Conclusions

PBLH sometimes differs from MLH over the ocean, making it crucial to estimate the PBLH in addition to the MLH. In this study, we used 506 dropsondes from NASA's ACTIVATE field campaigns over the northwest Atlantic from 2020 to 2022 to estimate PBLH and MLH. The PBLH and MLH differences are higher in winter (January, February, and March) than in other months (May, June, August, and September) because the PBL is more statically unstable and cloudier in winter.

These data were then used to evaluate the MLH product of airborne High-Spectral-Resolution Lidar—Generation 2 (HSRL-2). The HSRL-2 MLH product agrees well with MLH-dropsonde, with a median difference of 18 m and an  $R^2$  of 0.44. However, using the MLH-HSRL product to represent PBLH, as used in prior studies (e.g., for model evaluations), would introduce larger differences, with a median difference of −47 m.

We modified the automated wavelet-based MLH-HSRL algorithm for PBLH retrieval (i.e., PBLH-UA). The use of an automated algorithm also indicates the possibility of efficient retrieval of global PBLH in future satellite missions. The PBLH-UA performs better than MLH-HSRL in comparison with PBLH-dropsonde, with a median difference of −8 m and  $R^2$  of 0.48 (vs. −47 m and 0.42 for MLH-HSRL). These results demonstrate the potential of using HSRL-2 aerosol backscatter data to estimate both marine MLH and PBLH and suggest that lidar-derived MLH should be compared with radiosonde/dropsonde-determined MLH (not PBLH) in general.

These conclusions remain the same for cases with higher-or-lower low cloud fraction values, and for decoupled PBLs. As low cloud fraction increases, the differences between PBLH-dropsonde and MLH-dropsonde usually increase and the differences between HSRL-2-retrieved products and those from dropsondes usually also increase. Compared with the results using all dropsondes in the data set, the differences between PBLH-dropsonde and MLH-dropsonde and the differences between HSRL-2-retrieved products and those from dropsondes become greater on average for decoupled PBLs.

Note that the PBLH-UA algorithm includes two revisions to the MLH-HSRL algorithm as discussed in Section 2.3, and hence has a similar limitation: the PBLH derived from the aerosol backscatter profile does not always correspond to that determined from thermodynamic profiles when aerosol structures within and/or above the PBL is complicated (particularly when clouds are present or decoupled PBL exists).

The manual revision of the MLH-HSRL product in 2020 is found to improve the performance in MLH retrieval. We are currently using these data to investigate the relationship of instantaneous low cloud fractions with thermodynamic conditions as an extension of the global monthly and seasonal data analysis in Cutler et al. (2022). Recognizing that various methods have been used in the past to determine MLH or PBLH from radiosondes or dropsondes (e.g., Li et al., 2021; Zeng et al., 2004), we will comprehensively compare various methods of determining marine PBLH in dropsondes (including ours, as detailed in Figure 3) using the ACTIVATE dropsonde data covering all seasons in 3 years in a separate study. It will also be interesting to test the robustness of our algorithms (for PBLH retrieval from HSRL-2 and for MLH and PBLH estimates from dropsondes) and conclusions using dropsonde and HSRL data from several previous and upcoming airborne campaigns, such as the Cloud, Aerosol and Monsoon Processes Philippines Experiment (CAMP<sup>2</sup>Ex) (Reid et al., 2023) and the Convective Processes Experiment—Cabo Verde (CPEX-CV) in the eastern tropical Atlantic (<https://espo.nasa.gov/cpex-cv/content/CPEX-CV>). The PBLH and MLH data from dropsondes and HSRL-2 can also be used to evaluate climate models.

### Data Availability Statement

The ACTIVATE Data used in this study can be obtained from ACTIVATE Science Team (2020) and downloaded at <https://www-air.larc.nasa.gov/missions/activate/index.html>; <https://doi.org/10.5067/SUBORBITAL/ACTIVATE/DATA001>. The collocated PBLH-dropsonde, PBLH-UA, MLH-dropsonde, and MLH-HSRL data are available as tables at the above ACTIVATE website and at <https://www-air.larc.nasa.gov/cgi-bin/ArcView/activate.2019?ANALYSIS=1#XU.YIKE/>. Algorithm details are provided via flowcharts and explanations, and they are available from the authors.

### Acknowledgments

This work was funded by NASA Grant 80NSSC19K0442 in support of ACTIVATE, which is an Earth Venture Suborbital-3 (EVS-3) investigation funded by NASA's Earth Science Division and managed through the Earth System Science Pathfinder Program Office. We dedicate this work to the memory of coauthors Rodrigo Delgado and Claire E. Robinson.

### References

- ACTIVATE Science Team. (2020). Aerosol cloud meteorology interactions over the western Atlantic experiment data [Dataset]. *NASA Langley Atmospheric Science Data Center Distributed Active Archive Center*. <https://doi.org/10.5067/SUBORBITAL/ACTIVATE/DATA001>
- Bretherton, C. S., & Wyant, M. C. (1997). Moisture transport, lower-tropospheric stability, and decoupling of cloud-topped boundary layers. *Journal of the Atmospheric Sciences*, 54(1), 148–167. [https://doi.org/10.1175/1520-0469\(1997\)054<0148:mltsa>2.0.co;2](https://doi.org/10.1175/1520-0469(1997)054<0148:mltsa>2.0.co;2)
- Brooks, I. M. (2003). Finding boundary layer top: Application of a wavelet covariance transform to lidar backscatter profiles. *Journal of Atmospheric and Oceanic Technology*, 20(8), 1092–1105. [https://doi.org/10.1175/1520-0426\(2003\)020<1092:fbtao>2.0.co;2](https://doi.org/10.1175/1520-0426(2003)020<1092:fbtao>2.0.co;2)
- Brunke, M. A., Cutler, L., Urzua, R. D., Corral, A. F., Crosbie, E., Hair, J., et al. (2022). Aircraft observations of turbulence in cloudy and cloud-free boundary layers over the western North Atlantic Ocean from activate and implications for the Earth system model evaluation and development. *Journal of Geophysical Research: Atmospheres*, 127(19), e2022JD036480. <https://doi.org/10.1029/2022jd036480>
- Caicedo, V., Rappenglueck, B., Cuchiara, G., Flynn, J., Ferrare, R., Scarino, A. J., et al. (2019). Bay breeze and sea breeze circulation impacts on the planetary boundary layer and air quality from an observed and modeled DISCOVER-AQ Texas case study. *Journal of Geophysical Research: Atmospheres*, 124(13), 7359–7378. <https://doi.org/10.1029/2019jd030523>
- Cutler, L., Brunke, M. A., & Zeng, X. (2022). Re-evaluation of low cloud amount relationships with lower-tropospheric stability and estimated inversion strength. *Geophysical Research Letters*, 49(12), e2022GL098137. <https://doi.org/10.1029/2022gl098137>
- Davis, K. J., Gamage, N., Hagelberg, C. R., Kiemle, C., Lenschow, D. H., & Sullivan, P. P. (2000). An objective method for deriving atmospheric structure from airborne lidar observations. *Journal of Atmospheric and Oceanic Technology*, 17(11), 1455–1468. [https://doi.org/10.1175/1520-0426\(2000\)017<1455:aomfda>2.0.co;2](https://doi.org/10.1175/1520-0426(2000)017<1455:aomfda>2.0.co;2)
- Garratt, J. R. (1992). *The atmospheric boundary layer*. Cambridge University Press.
- Hair, J. W., Hostetler, C. A., Cook, A. L., Harper, D. B., Ferrare, R. A., Mack, T. L., et al. (2008). Airborne high spectral resolution lidar for profiling aerosol optical properties. *Applied Optics*, 47(36), 6734. <https://doi.org/10.1364/ao.47.006734>
- Hegarty, J. D., Lewis, J., McGrath-Spangler, E. L., Henderson, J., Scarino, A. J., DeCola, P., et al. (2018). Analysis of the planetary boundary layer height during DISCOVER-AQ Baltimore–Washington, D.C., with lidar and high-resolution WRF modeling. *Journal of Applied Meteorology and Climatology*, 57(11), 2679–2696. <https://doi.org/10.1175/jamc-d-18-0014.1>
- Hunt, W. H., Winker, D. M., Vaughan, M. A., Powell, K. A., Lucker, P. L., & Weimer, C. (2009). Calipso lidar description and performance assessment. *Journal of Atmospheric and Oceanic Technology*, 26(7), 1214–1228. <https://doi.org/10.1175/2009jtecha1223.1>
- Jones, C. R., Bretherton, C. S., & Leon, D. (2011). Coupled vs. decoupled boundary layers in VOCALS-REx. *Atmospheric Chemistry and Physics*, 11(14), 7143–7153. <https://doi.org/10.5194/acp-11-7143-2011>
- Kirschler, S., Voigt, C., Anderson, B. E., Chen, G., Crosbie, E. C., Ferrare, R. A., et al. (2023). Overview and statistical analysis of boundary layer clouds and precipitation over the western North Atlantic Ocean. *Atmospheric Chemistry and Physics*, 23(18), 10731–10750. <https://doi.org/10.5194/acp-23-10731-2023>
- Li, H., Liu, B., Ma, X., Jin, S., Ma, Y., Zhao, Y., & Gong, W. (2021). Evaluation of retrieval methods for planetary boundary layer height based on radiosonde data. *Atmospheric Measurement Techniques*, 14(9), 5977–5986. <https://doi.org/10.5194/amt-14-5977-2021>

- Liu, X., Wang, Y., Wasti, S., Li, W., Soleimani, E., Flynn, J., et al. (2023). Evaluating WRF-GC v2.0 predictions of boundary layer height and vertical ozone profile during the 2021 TRACER-AQ campaign in Houston, Texas. *Geoscientific Model Development*, *16*(18), 5493–5514. <https://doi.org/10.5194/gmd-16-5493-2023>
- Luo, T., Wang, Z., Zhang, D., & Chen, B. (2016). Marine boundary layer structure as observed by A-train satellites. *Atmospheric Chemistry and Physics*, *16*(9), 5891–5903. <https://doi.org/10.5194/acp-16-5891-2016>
- Neumann, T. A., Martino, A. J., Markus, T., Bae, S., Bock, M. R., Brenner, A. C., et al. (2019). The ice, cloud, and land elevation satellite—2 mission: A global geolocated photon product derived from the advanced topographic laser altimeter system. *Remote Sensing of Environment*, *233*, 111325. <https://doi.org/10.1016/j.rse.2019.111325>
- Palm, S. P., Selmer, P., Yorks, J., Nicholls, S., & Nowotnick, E. (2021). Planetary boundary layer height estimates from ICESat-2 and CATS backscatter measurements. *Frontiers in Remote Sensing*, *2*. <https://doi.org/10.3389/frsen.2021.716951>
- Reid, J. S., Maring, H. B., Narisma, G. T., van den Heever, S., Di Girolamo, L., Ferrare, R., et al. (2023). The coupling between tropical meteorology, aerosol lifecycle, convection, and radiation during the cloud, aerosol and monsoon processes Philippines experiment (CAM-P2Ex). *Bulletin of the American Meteorological Society*, *104*(6), E1179–E1205. <https://doi.org/10.1175/BAMS-D-21-0285.1>
- Scarino, A. J., Obland, M. D., Fast, J. D., Burton, S. P., Ferrare, R. A., Hostetler, C. A., et al. (2014). Comparison of mixed layer heights from airborne high spectral resolution LIDAR, ground-based measurements, and the WRF-Chem model during CalNex and CARES. *Atmospheric Chemistry and Physics*, *14*(11), 5547–5560. <https://doi.org/10.5194/acp-14-5547-2014>
- Sorooshian, A., Alexandrov, M. D., Bell, A. D., Bennett, R., Betito, G., Burton, S. P., et al. (2023). Spatially coordinated airborne data and complementary products for aerosol, gas, cloud, and meteorological studies: The NASA activate dataset. *Earth System Science Data*, *15*(8), 3419–3472. <https://doi.org/10.5194/essd-15-3419-2023>
- Sorooshian, A., Anderson, B., Bauer, S. E., Braun, R. A., Cairns, B., Crosbie, E., et al. (2019). Aerosol–cloud–meteorology interaction airborne field investigations: Using lessons learned from the U.S. West Coast in the design of activate off the U.S. East Coast. *Bulletin of the American Meteorological Society*, *100*(8), 1511–1528. <https://doi.org/10.1175/bams-d-18-0100.1>
- Teixeira, J., Piepmeier, J., & Nehrir, A. (2020). NASA incubation study on planetary boundary layer. In *IGARSS 2020–2020 IEEE international geoscience and remote sensing symposium*. <https://doi.org/10.1109/igarss39084.2020.9323101>
- Tornow, F., Ackerman, A. S., Fridlind, A. M., Tselioudis, G., Cairns, B., Painemal, D., & Elsaesser, G. (2023). On the impact of a dry intrusion driving cloud-regime transitions in a midlatitude cold-air outbreak. *Journal of the Atmospheric Sciences*, *80*(12), 2881–2896. <https://doi.org/10.1175/jas-d-23-0040.1>
- Vömel, H., Sorooshian, A., Robinson, C., Shingler, T. J., Thornhill, K. L., & Ziemba, L. D. (2023). Dropsonde observations during the aerosol cloud meteorology interactions over the western Atlantic Experiment. *Scientific Data*, *10*(1), 753. <https://doi.org/10.1038/s41597-023-02647-5>
- Wood, R., & Bretherton, C. S. (2004). Boundary layer depth, entrainment, and decoupling in the cloud-capped subtropical and tropical marine boundary layer. *Journal of Climate*, *17*(18), 3576–3588. [https://doi.org/10.1175/1520-0442\(2004\)017<3576:bldead>2.0.co;2](https://doi.org/10.1175/1520-0442(2004)017<3576:bldead>2.0.co;2)
- Zeng, X., Brunke, M. A., Zhou, M., Fairall, C., Bond, N. A., & Lenschow, D. H. (2004). Marine atmospheric boundary layer height over the eastern pacific: Data analysis and model evaluation. *Journal of Climate*, *17*(21), 4159–4170. <https://doi.org/10.1175/jcli3190.1>
- Zuidema, P., Painemal, D., de Szoeko, S., & Fairall, C. (2009). Stratocumulus cloud-top height estimates and their climatic implications. *Journal of Climate*, *22*(17), 4652–4666. <https://doi.org/10.1175/2009jcli2708.1>